International Journal of Refractory Metals and Hard Materials 112 (2023) 106155

Contents lists available at ScienceDirect

International Journal of Refractory Metals and Hard Materials

journal homepage: www.elsevier.com/locate/IJRMHM

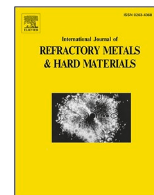

Digital image correlation after focused ion beam micro-slit drilling: A new technique for measuring residual stresses in hardmetal components at local scale

A. Dorronsoro [a,b,*], J. Navarrete [a,b], A. Pan [a,b], E. Castaño [a,b], J.M. Sánchez [a,b], J. Alkorta [a,b]

[a] CEIT-BRTA, Paseo Manuel Lardizabal 15, Donostia 20018, Spain
[b] Universidad de Navarra, Tecnun, Paseo Manuel Lardizabal 13, Donostia 20018, Spain

ARTICLE INFO

Keywords:
WC-Co hardmetals
Residual stress
Digital image correlation
Micro-slit drilling
Femto-laser machining

ABSTRACT

A new method has been developed for measuring residual stresses at the surface of hardmetal components with higher spatial resolution than standard X-ray diffraction methods. It is based on measuring the surface displacements produced when stresses are partially released by machining a thin slit perpendicularly to the tested surface. Slit machining is carried out by focused ion beam (FIB). Measurement of the displacement fields around the FIB slit are performed by applying an advanced digital image correlation algorithm based on Fourier analysis with sub-pixel resolution. This method compares SEM images of the same area of the hardmetal surface before and after slitting. The method has been successfully applied to as-ground and femto-laser textured surfaces showing good correlation with the standard $\sin^2\psi$ XRD technique. It is concluded that texturing induced by laser pulses in the femtoseconds regime is not perfectly adiabatic, since residual stresses are reduced by 15%.

1. Introduction

Residual stresses are critical for the performance of hardmetal tools, especially under fatigue [1]. They arise from local differences in, for example, thermal expansion coefficient, stiffness, yield stress between the different phases present in the material or deformation gradients during shaping [2]. The presence of these stresses can cause crack initiation or damage accumulation, which will often lead to premature tool failure. On the other hand, an appropriate introduction of these stresses can improve fatigue resistance by inducing compressive stresses that delay crack formation (i.e. grinding operations). Many edge preparation techniques rely on this fact inducing such compressive residual stresses by special microblasting operations [3].

Various residual stress measurement methods exist, valid for different length scales [2]. For macro-scale stresses, hole-drilling or crack compliance methods are widely used. They rely on monitoring distortions on the sample caused by stress relaxation via strain gauges or optical methods, while or after mechanically removing part of the material. On the other hand, diffraction based methods allow the measurement of stresses at smaller scales and are non-destructive. Although spatial resolution and accuracy depend on the type of radiation applied, X-ray diffraction (XRD) methods are the most commonly used due to their higher availability compared to neutron or high energy X-ray sources. Among them, the so-called $\sin^2\psi$ technique provides a spatial resolution of around $50 \times 50\ \mu m^2$, a probed depth of approx. 5 μm in the case of WC-materials and the stress accuracy of $\approx \pm 50$ MPa [4]. If higher resolution is needed, for example, for analysing the stress state at few microns away from the cutting edge, XRD are not valid. High resolution electron backscattering diffraction (HR-EBSD) has been employed for the determination of lattice microstresses from EBSD patterns at the micron scale achieving a strain sensitivity of $\sim 2 \times 10^{-4}$ [5–7]. However, these techniques require a careful preparation of the surface not applicable to standard hardmetal ground specimens. Alternatively, hole-drilling methods are presently being investigated for measuring residual stresses at micro-scale level [8–12]. These techniques are referred to as "FIB-DIC" and are based on releasing the residual stresses from a surface by means of a focused ion beam (FIB) gun and measuring the corresponding deformations by applying digital image correlation (DIC) to scanning electron images taken before and after machining. The aim of the present article is to develop a FIB-DIC methodology suitable for measuring residual surfaces in hardmetal machined surfaces. The method will be applied either to surfaces ground with standard diamond

* Corresponding author at: CEIT-BRTA, Paseo Manuel Lardizabal 15, Donostia 20018, Spain.
E-mail addresses: adlarbide@ceit.es (A. Dorronsoro), jnavarrete@ceit.es (J. Navarrete), apan@ceit.es (A. Pan), ecastano@ceit.es (E. Castaño), jmsanchez@ceit.es (J.M. Sánchez), jalkorta@ceit.es (J. Alkorta).

https://doi.org/10.1016/j.ijrmhm.2023.106155
Received 2 December 2022; Received in revised form 13 February 2023; Accepted 13 February 2023
Available online 15 February 2023
0263-4368/© 2023 The Authors. Published by Elsevier Ltd. This is an open access article under the CC BY-NC-ND license (http://creativecommons.org/licenses/by-nc-nd/4.0/).

wheels or to nano-textured surfaces processed by ultra-short pulsed laser machining. The latter technology is presently being developed for improving lubricant retention without inducing significant thermal damage [13].

2. Experimental procedure

(a) Generation of residual stresses.

Hardmetal specimens selected for this investigation correspond to a WC-10wt.%Co submicron grade with a density of 14.35 g/cm^3 (ISO-3369), a Vickers hardness of 1675 ± 20 kg/mm^2 (HV30, ISO-3878) and an estimated Young's modulus and Poisson ratio of 584 GPa and 0.21 respectively [14]. Samples were ground with a diamond grinding wheel (D91-C100 from Norton) at a linear speed of 18 m/s, a feed of 0.25 mm/s and a depth of cut of 2 mm for inducing a high compressive surface residual stress state. Samples were directly pressed, sintered and ground without any cutting or other sample preparation.

Subsequently, surface residual stresses were modified by using a pulsed laser with a wavelength of 1030 nm, a pulse duration of 280 fs and a spot size of 30 μm. Two conditions were tested on surface areas of 3 × 3 mm^2. Condition 1: 20 pulses at 1 W and Condition 2: 10 pulses at 2 W. In both cases, the total fluence was 4.8 J/cm^2. An example of the textures obtained by applying these conditions is shown in Fig. 1. These laser-induced-periodic-surface-structures (LIPSS) have spatial periods ranging from tens to hundreds of nanometres, always shorter than the wavelength of the laser used in their generation [15,16].

(b) Reference method for measuring residual stresses.

The sin^{2}ψ XRD technique was selected as the reference method for measuring these residual stresses. The diffraction setup was based on the Bragg-Brentano configuration using point focus, a diffraction window of 1 × 1 mm^2 and secondary optics based on combining a monochromator and a collimator. Stresses were measured on the WC phase using the (3,0,0) crystal plane and Cu radiation (2θ = 133°) for increasing sensitivity [4]. Under these conditions, X-ray penetration depth calculated with Bruker software is 4.0 μm.

(c) Focused ion beam machining (FIB)

FIB machining was carried out with a Ga^+ ion gun at 30 kV with a milling current of 3 nA. In all experiments, the surface of incidence of Ga ions was a rectangle of 50 × 1 μm^2. The FIB system does not consider the material, so its depth estimate is not accurate. A depth calibration was therefore carried out. Different milling depths ("h") were obtained by increasing the milling time from 2 to 32 min in increasing powers of two, and then milling a cross section perpendicular to the slits to observe the depth (Fig. 2). As seen in the higher magnification image included in the bottom left corner, cross section slit profiles perpendicular to the longer slit side are close to an isosceles triangle. The effect of applied ion current on the slit depth is shown in Fig. 3.

After these calibration experiments, the final dimensions selected for the FIB slits were 50 × 1 × 5 μm^3 to be consistent with the calculated penetration of X-rays during the diffraction experiments. Slits were milled in three regions using a milling current of 3 nA. Higher milling currents have a stronger influence on the regions surrounding the slit and cause larger alterations of the imaging area (such as contrast changes in the areas with higher deposition of Ga^+ ions) [17,18]. The target depth was 5 μm, so the milling time was set to 3 min and 40 s.

Depth calibration took close to 15 h (most of which consisted of autonomous work of the microscope). Once the milling parameters were selected, less than an hour was needed for each measurement: ~15 min for image acquisition (accounting for the time needed to focus, adjust stigmatism, etc.) before and after FIB milling, ~15 min to adjust and focus the ion beam, and 3 min and 40 s milling each slit.

3. Data analysis

The methodology proposed for measuring residual stresses both in ground and laser treated hardmetal surfaces is based on comparing the secondary electron scanning electron microscope (SE-SEM) images obtained before and after FIB slitting. The main novelty of this work is the development of an alternative digital image correlation algorithm based on Fourier analysis for calculating the corresponding surface displacement fields around the slit. On a second step, a finite element (FE) model has been developed for calculating the corresponding stresses, assuming that the hardmetal behaves like a continuous material with the elastic properties included in section 2a.

(a) Fourier-based DIC.

The key difference between the DIC approach in this paper and the standard correlation method is the use of Fourier analysis. Feature-based correlation methods calculate the degree of correlation (quality of match) between the two images (or areas within the images) for multiple possible shift values, and choose the value that yields the maximum correlation. For images with multiple features (different objects, lighting patterns, etc.) this method works correctly, because the more features that need to be matched, the more obvious the point of maximum correlation will be. On the other hand, pictures that do not have many easily recognisable areas are harder to adjust using this approach. Additionally, if some features in the image present local periodicity, multiple local peaks (related to the period of the repeating pattern) could be present in the correlation maps, thus making the maximum value difficult to calculate.

In order to solve these two potential problems, a speckle pattern can be applied to the surface. This pattern should form a randomly

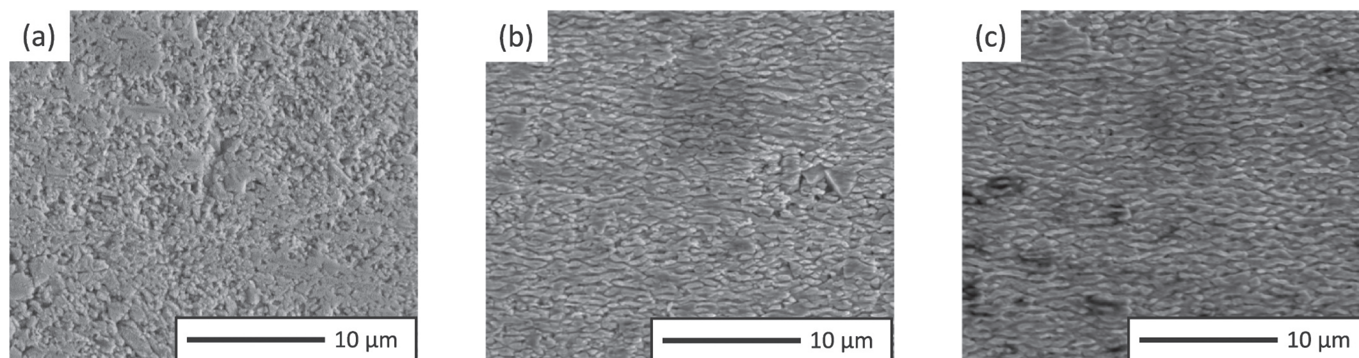

Fig. 1. SE-SEM images corresponding to WC-10wt.%Co submicron grade: (a) as-ground condition, (b) after ultrashort pulsed laser treatment, Condition 1 and (c) Id., Condition 2.

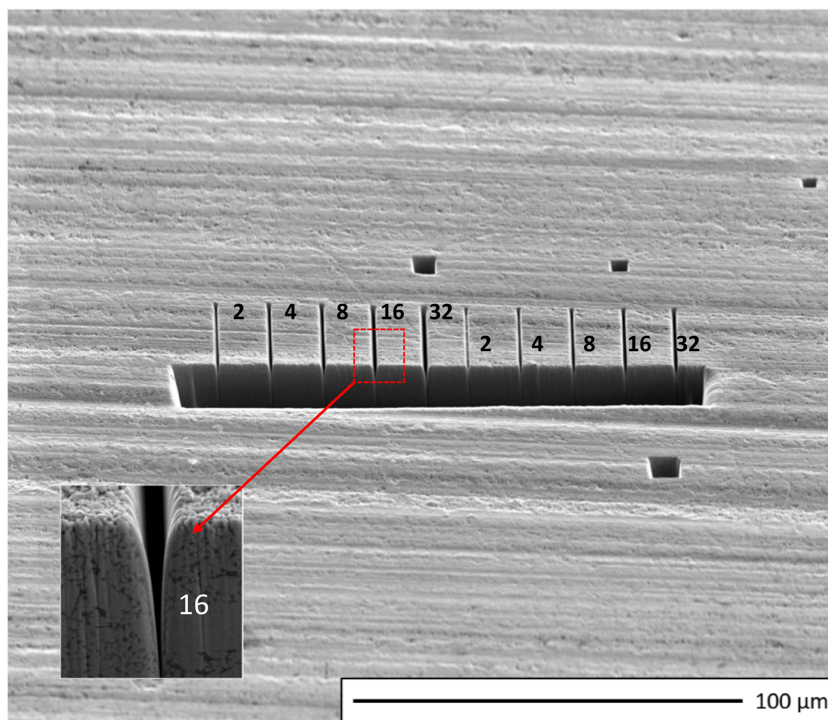

Fig. 2. SE-SEM image showing a cross-section of 10 FIB-machined slits parallel to each other. Slit dimensions: $50 \times 1\ \mu m^2$ with different milling times. Numbers on the right of each slit indicate the milling time in minutes. The five on the left correspond to a FIB current of 7 nA and the five on the right to 3 nA. The inset in the bottom left corner shows a close-up of one of the slits.

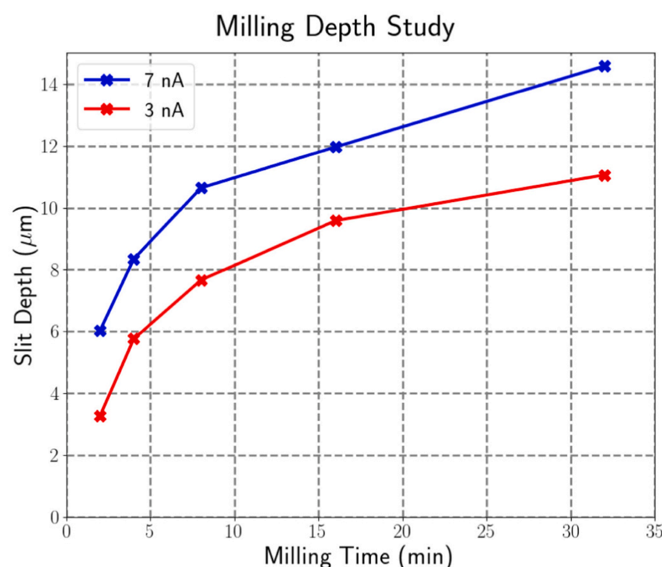

Fig. 3. Slit depths (h) as a function of milling time for two milling currents: 3 nA (in red) and 7 nA (in blue). (For interpretation of the references to colour in this figure legend, the reader is referred to the web version of this article.)

distributed arrangement of features (for instance, dots of different sizes) that offer high contrast and resolve uniqueness issues. An example of a gold nanoparticle speckle pattern for SEM imaging is given in reference [19]. The size of the applied pattern limits the resolution capability of the algorithm. Furthermore, the stiffness of the coating itself can have an influence on the measurement.

SEM images of a surface are subject to these imaging problems: many microstructural features can have periodic regions (for example, a eutectoid steel with a periodic ferrite-cementite lamellar structure), homogeneous in size or just not frequent enough to guarantee good correlation measurement.

Fourier-based digital image correlation [20] relies on a different approach to find the relative displacement between images, more sensitive in the presence of subtle features. If $I_1\ (x,y)$ and $I_2\ (x,y)$ represent the pixel intensity values for two images that are identical with the exception of a coordinate shift, so that $I_2\ (x,y) = I_1\ (x - x_0, y - y_0)$, their Fourier transforms relate this way:

$$F_2(\xi,\eta) = e^{-i(\xi x_0 + \eta y_0)} F_1(\xi,\eta) \tag{1}$$

This is known as the Fourier shift theorem. It is easy to see that if the phase term is isolated and the inverse Fourier transform is applied, we obtain a Dirac's delta with its origin at (x_0, y_0):

$$\mathrm{F}^{-1}\left\{\frac{F_1(\xi,\eta)F_2^*(\xi,\eta)}{|F_1(\xi,\eta)F_2^*(\xi,\eta)|}\right\} = \mathrm{F}^{-1}\left\{e^{i\ (\xi x_0 + \eta y_0)}\right\} = \delta(x - x_0, y - y_0) \tag{2}$$

where $F_2{}^*$ stands for the complex conjugate of the Fourier transform of image 2.

Real images are finite and contain a certain degree of noise, so a finite peak (instead of Dirac's delta) is expected at the position corresponding to the displacement value (x_0, y_0). Sub-pixel resolution of image shift (~0.05 pixels) can be achieved using these measurement techniques [21].

The normalisation term (denominator) in Eq. (2) gives equal weight to all components in the Fourier transforms of the images, even those that are not representative of features, which makes this approach sensitive to noise [22,23]. Consequently, the expression has been adapted to include an exponent in the denominator, so that the contribution of noise becomes less significant:

$$P(x,y) = \mathrm{F}^{-1}\left\{\frac{F_1(\xi,\eta)F_2^*(\xi,\eta)}{|F_1(\xi,\eta)F_2^*(\xi,\eta)|^n}\right\} \tag{3}$$

$n = 0$ corresponds to the Simple Correlation case, and $n = 1$ becomes

Eq. (2), also called Phase Correlation. In this paper, an exponent value of $n = 0.75$ was used.

A Fourier-based DIC calculation can therefore be carried out by performing these operations: Fourier transform of both images, the product and division operations described in Eq. (3), calculating its inverse Fourier transform and finding the peak of the resulting distribution.

Other exploration-based algorithms repeat their calculations with various shift values in order to find the maximum correlation, which might require more operations for larger displacements. With this approach, the computational steps are independent of the magnitude of the displacement and are determined by the size of the image. Fast Fourier Transform (FFT) algorithms [24] make these operations computationally efficient.

The algorithm used in this paper also uses an edge enhancer operation: pixel intensity gradients are calculated in the vertical and horizontal directions and saved as the real and imaginary part of a complex image G, as follows:

$$G(x, y) = \nabla_x I(x, y) + i\, \nabla_y I(x, y) \tag{4}$$

where $I(x,y)$ is the reference image. Instead of working with the pixel intensities of images directly, the correlation between $G_1(x,y)$ and $G_2(x,y)$ is calculated, as explained in [25]. An example of such an enhanced edge map of a SEM micrograph image is shown in Fig. 4. By storing both gradient maps as the real and imaginary part of the image, more detailed edge information is available to perform the correlation calculation. A pre-processing filtering step is carried out in order to reduce image noise and improve gradient operations.

The DIC algorithm requires images of the same area before and after milling. The milling process is performed with a tilted sample stage (52° in FEI Quanta 3D FEG), and it requires some stage movement to focus the beam before the process. Consequently, the position of the stage has to be adjusted to match the same area. The small displacements produced during this adjustment are corrected by performing an initial DIC global image identification. The SEM images used in this paper have a resolution of 4096 × 3773 square pixels, and a horizontal field width (real width of the region in the image) of 149 μm, so every pixel represents an area of approximately 36 × 36 nm^2.

After the global image adjusting step that corrected the possible mismatch caused by the stage movement in between captures, the image was sliced in multiple smaller regions, each called region of interest (ROI). These ROIs were 64 × 64 square pixels. The shift of each region was then calculated using the DIC algorithm, to construct a displacement map. Construction of the displacement map is the most computationally expensive step in the data manipulation process, and it takes close to 10 min. These displacement maps can be influenced by sample drift, caused by build-up of electrical charge during the imaging. This factor can be reduced by choosing faster scan times (which increases noise) and averaging many images (to compensate for the introduced noise) but, unfortunately, it cannot be completely eliminated. In the DIC algorithm, the influence of sample drift is estimated and corrected.

Images included in Fig. 5 show one example of the results obtained following this procedure. Fig. 5a corresponds to the as-ground surface region to be tested. Fig. 5b shows the position of the FIB machined slit and the corresponding surface displacement map. Red shading represents downward displacements of the hardmetal surface perpendicularly to the slit's longer side and blue shading relates to displacements in the opposite direction. This means that residual stresses are of compressive nature since surface displacements tend to close the slit. As expected, maximum displacements are measured at the slit centre.

Fig. 6 shows the SEM images of the areas textured with Conditions 1 (6a) and 2 (6b) (see section 2a) after FIB slitting, also combined with the corresponding displacement maps. The displacement map obtained in the area textured with Condition 2 (the one that used 2 W laser pulses) contains considerably more noise.

(b) FE simulations.

A FE model has been developed for reproducing the surface displacement field obtained by Fourier based DIC using ABAQUS software (Dassault Systèmes). The slit geometry was defined with the same triangular cross-section found experimentally (Fig. 7a). The slit length was 100 times smaller than the size of the whole model, to ensure that the boundaries would not affect the stress evolution near the slit. The aspect ratios between length l, width w and depth h of the slit were $l/w = 50$ and $l/h = 10$. Due to the symmetry of the system, only half of the slit was modelled, and symmetry boundary conditions were imposed in the centre face. A mesh containing 485,874 3D tetragonal (C3D10) elements was used, fine around the slit and gradually coarser at larger distances (Fig. 7b).

An initial state of homogeneous biaxial compressive stress of 1 GPa ($\sigma/E = 1/584$) was imposed as initial condition and then the system was allowed to relax. The material was assumed linear elastic with Young's modulus and Poisson ratio given in section 2a. This linear elastic nature of unloading is expected to hold not only for hardmetals but also for other materials, including most metals and ceramics.

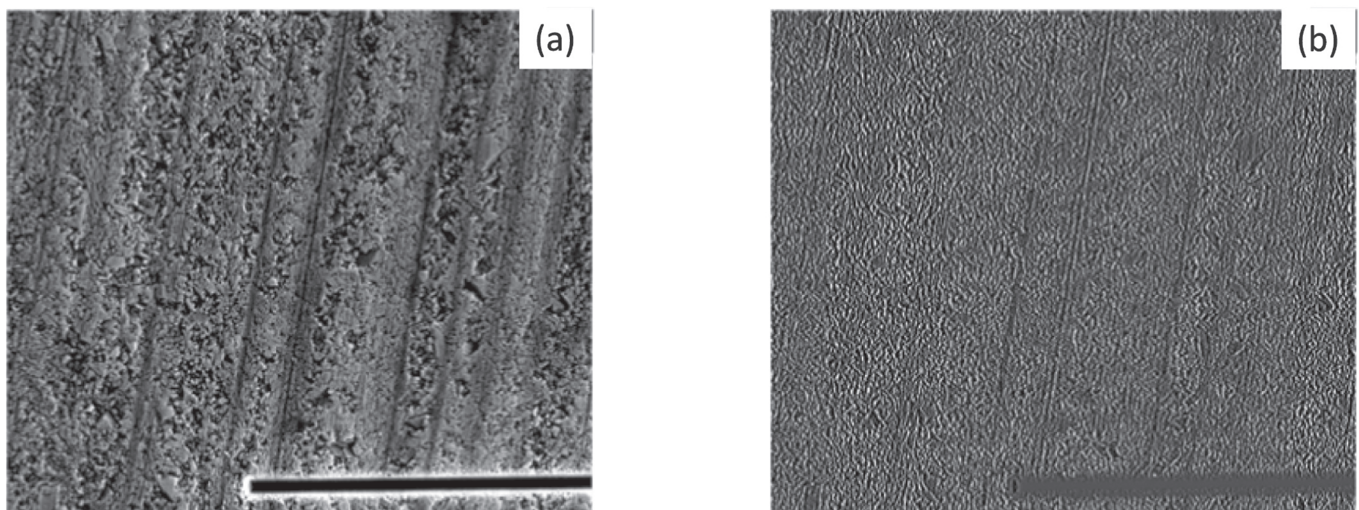

Fig. 4. (a) SE-SEM image of the sample surface and (b) its horizontal gradient where the edges of the micrograph are enhanced.

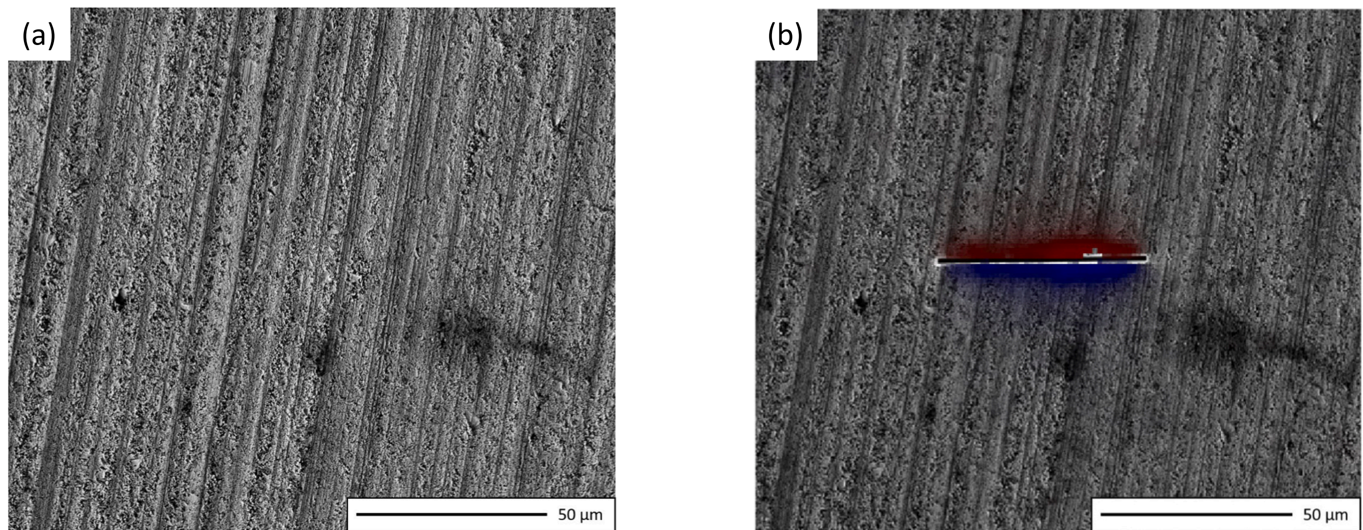

Fig. 5. SE-SEM images of the hardmetal surface in as-ground state: (a) before FIB slit milling and (b) after FIB slit milling. The shading corresponds to the displacements measured with DIC (red: downward, blue: upward). (For interpretation of the references to colour in this figure legend, the reader is referred to the web version of this article.)

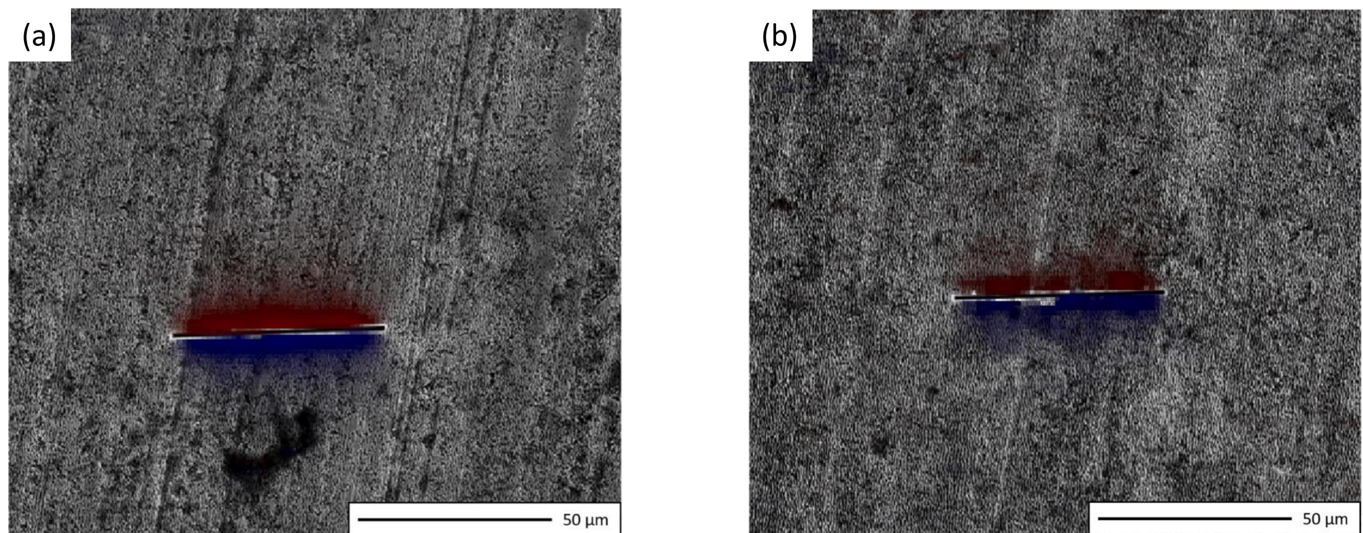

Fig. 6. SE-SEM image showing the surface displacement map calculated with Fourier-DIC algorithm for the case of the LIPSS textured surfaces. (a) Condition 1. (b) Condition 2. The shading corresponds to the displacements measured with DIC (red: downward, blue: upward). (For interpretation of the references to colour in this figure legend, the reader is referred to the web version of this article.)

4. Results and discussion

The fitting of FE deformation profiles to the Fourier-DIC calculated displacement maps is shown in Fig. 8. The high spatial resolution of the technique is noticeable: the maximum detected displacements were of about 40 nm, while the length of each pixel is of the order of 36 nm. It is worth noting that the deformations decay sharply from the slit border, vanishing almost completely at distances of about 40 µm.

Table 1 summarises the numerical values of residual stresses with $\sin^2\psi$ XRD and FIB-DIC techniques. In both cases, errors correspond to 95% confidence intervals. In FIB-DIC method, 95% confidence intervals are those corresponding to the fitting between FE strain profiles and FIB-DIC surface deformation maps (Fig. 8). There is excellent agreement between results obtained by the two techniques in as-ground and laser treated surfaces in Condition 1 (i.e. with less intense laser pulses). For the surface treated in Condition 2, the values obtained with FIB-DIC technique are 20% lower. This discrepancy is likely related to interaction between the generated texture and the displacement field around the FIB slit, which are similar in magnitude. Therefore, displacement fields are much noisier in this experiment (Fig. 6b). Optimised filtering procedures are under current research. Another possible explanation is the difference in depth-resolution of the methods. While XRD measurements probe about 5 µm of the surface, the stress relaxation process caused by the slit happens in a smaller region. The slit itself is 5 µm deep, where displacements must gradually vanish, so that the measurement represents the stress state of a shallower region.

Apart from comparing the new FIB-DIC technique with the standard $\sin^2\psi$ XRD procedure, these results show that, although femto pulsed laser machining is considered a nearly adiabatic process this is not completely true. Generation of nanometric structures (LIPSS type) involves very small material removal, especially in Condition 1 and certain surface annealing is produced with approx. 15% reduction of residual stresses. Anyhow, these are still highly compressive and far from the annealed condition.

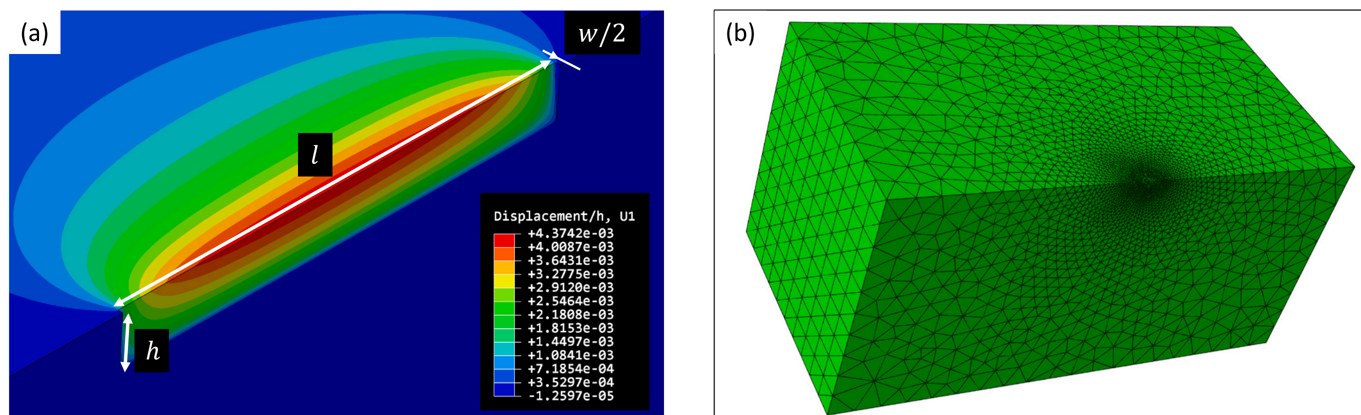

Fig. 7. (a) FE-simulated displacement profile for a linear elastic system with compressive residual stresses. Displacements (normalised to slit depth) are shown in the direction perpendicular to the slit's longest side, where unloading is maximum. (b) Mesh of the model used in the FE simulation, containing 485,874 C3D10 tetragonal elements.

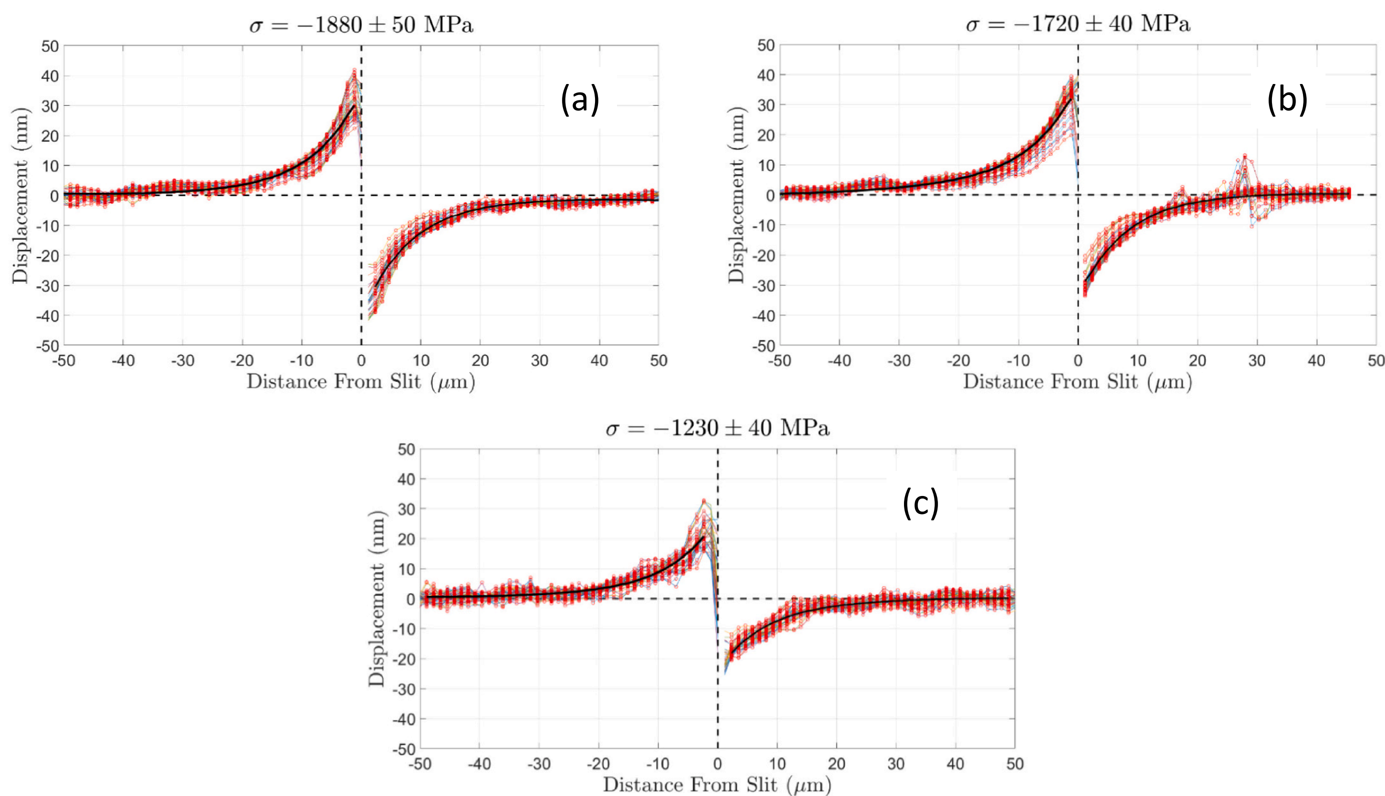

Fig. 8. Fitting of Fourier-DIC-measured displacements to FE data: (a) as-ground surface, (b) Ultrashort pulsed laser texturing, condition 1 and (c) Id. Condition 2. Red dots represent DIC-calculated displacements, and the black solid lines correspond to the fitting of the FE simulations. (For interpretation of the references to colour in this figure legend, the reader is referred to the web version of this article.)

Table 1
Residual stress values measured with $\sin^2\psi$ XRD and Fourier-based FIB-DIC techniques.

Surface condition	Residual stress (MPa)	
	$\sin^2\psi$ XRD	FIB-DIC
As-ground	−1940 ± 150	−1880 ± 50
Laser textured Condition 1	−1700 ± 130	−1720 ± 40
Laser textured Condition 2	−1540 ± 130	−1230 ± 40

5. Conclusions

Surface residual stresses in hardmetals have a critical effect on their mechanical performance. For the first time, a new FIB-DIC method has been implemented for measuring residual stresses with spatial resolutions 1 order of magnitude lower than those achieved by standard X-ray diffraction methods. The new procedure is based on machining a thin slit perpendicular to the surface of interest by means of a focused ion beam equipment. As stresses are released, surface displacements occur near the slit edges. These displacements are measured by an advanced digital image correlation algorithm to SEM images taken before and after slitting. This algorithm, based on Fourier analysis, can reach sub-pixel

resolution and the processing time is only dependent on the size of the image. Finally, residual stresses are obtained by fitting the FIB-DIC measured displacements to FE-simulated stress-relief curves.

Once calibrated, the FIB-DIC method has been applied to as-ground and laser textured hardmetal surfaces. Compressive residual stresses produced by grinding are reduced by ultrashort pulsed laser texturing. This stress relaxation depends more on the individual fluence of laser pulses than on the total fluence of the whole texturing process. Correlation between FIB-DIC and $\sin^2\psi$ techniques is excellent for as-ground and low power laser texturing, being worse when texturing is carried out with power of individual pulses increases. Apart from its higher spatial resolution, the new FIB-DIC technique has the advantage of being suitable for amorphous materials and for investigating stresses of hard coatings near the coating edge.

CRediT authorship contribution statement

A. Dorronsoro: Methodology, Software, Validation, Formal analysis, Investigation, Data curation, Writing – original draft, Visualization. **J. Navarrete:** Investigation. **A. Pan:** Investigation. **E. Castaño:** Resources. **J.M. Sánchez:** Resources, Writing – review & editing. **J. Alkorta:** Conceptualization, Writing – review & editing, Supervision, Project administration, Funding acquisition.

Declaration of Competing Interest

The authors declare that they have no known competing financial interests or personal relationships that could have appeared to influence the work reported in this paper.

Data availability

Data will be made available on request.

Acknowledgements

The authors would like to thank NV Bekaert SA for funding this research and for their continued support and valuable comments throughout the development of the work.

References

[1] A. Betzwar Kotas, H. Danninger, B. Weiss, K. Mingard, J.M. Sanchez, L. Llanes, Fatigue testing and properties of hardmetals in the gigacycle range, Int. J. Refract. Met. Hard Mater. 62 (2017) 183–191.
[2] P.J. Withers, H. Bhadeshia, Residual stress. part 1 – measurement techniques, Mater. Sci. Technol. 17 (4) (2001) 355–365.
[3] K.-D. Bouzakis, B. Skordaris, E. Bouzakis, A. Tsouknidas, S. Madrimallakis, S. Gerardis, G. Katirtzoglou, Optimization of wet micro-blasting on PVD films with various grain materials for improving the coated tools' cutting performance, CIRP Ann. 60 (1) (2011) 587–590.
[4] B.D. Cullity, Elements of X-Ray Diffraction, 2nd ed., Addison Wesley Pub. Co. Inc., 1978, pp. 447–478.
[5] A.J. Wilkinson, G. Meaden, D.J. Dingley, High-resolution elastic strain measurement from electron backscatter diffraction patterns: new levels of sensitivity, Ultramicroscopy 106 (4–5) (2006) 307–313.
[6] J. Alkorta, Limits of simulation based high resolution ebsd, Ultramicroscopy 131 (2013) 33–38.
[7] J. Alkorta, M. Marteleur, P.J. Jacques, Improved simulation based hr-ebsd procedure using image gradient based dic techniques, Ultramicroscopy 182 (2017) 17–27.
[8] A.J. Lunt, A.M. Korsunsky, A review of micro-scale focused ion beam milling and digital image correlation analysis for residual stress evaluation and error estimation, Surf. Coat. Technol. 283 (2015) 373–388.
[9] K. Kang, N. Yao, M. He, A. Evans, A method for in situ measurement of the residual stress in thin films by using the focused ion beam, Thin Solid Films 443 (1–2) (2003) 71–77.
[10] B. Winiarski, P. Withers, Micron-scale residual stress measurement by micro-hole drilling and digital image correlation, Exp. Mech. 52 (2012) 417–428.
[11] A.M. Korsunsky, M. Sebastiani, E. Bemporad, Residual stress evaluation at the micrometer scale: analysis of thin coatings by fib milling and digital image correlation, Surf. Coat. Technol. 205 (7) (2010) 2393–2403.
[12] M. Sebastiani, C. Eberl, E. Bemporad, G.M. Pharr, Depth-resolved residual stress analysis of thin coatings by a new fib–dic method, Mater. Sci. Eng. A 528 (27) (2011) 7901–7908.
[13] J.M. Sanchez Moreno, E. Castaño Carmona, A. Pan Cabo, L. Lozada Cabezas, J. Alkorta, T. Soria Biurrun, J. Navarrete Cuadrado, Surface texturing and edge treatment of hardmetal tools by means of femtosecond pulsed laser, in: 20th Plansee Seminar, Proc. of Int. Conf. on Refract. Met. and Hard Mat., HM93/1, Reutte/Austria, May 30-June 3 2022.
[14] A. Savinykh, K. Mandel, S. Razorenov, L. Krüger, The influence of the cobalt content on the strength properties of tungsten carbide ceramics under dynamic loads, Tech. Phys. 63 (2018) 357–362.
[15] A.Y. Vorobyev, C. Guo, Direct femtosecond laser surface nano/microstructuring and its applications, Laser Photonics Rev. 7 (3) (2013) 385–407.
[16] S. He, J.J. Nivas, K. Anoop, A. Vecchione, M. Hu, R. Bruzzese, S. Amoruso, Surface structures induced by ultrashort laser pulses: formation mechanisms of ripples and grooves, Appl. Surf. Sci. 353 (2015) 1214–1222.
[17] D. Kiener, C. Motz, M. Rester, M. Jenko, G. Dehm, Fib damage of cu and possible consequences for miniaturized mechanical tests, Mater. Sci. Eng. A 459 (1–2) (2007) 262–272.
[18] J. Hütsch, E.T. Lilleodden, The influence of focused ion beam preparation technique on microcompression investigations: lathe vs. annular milling, Scr. Mater. 77 (2014) 49–51.
[19] A.D. Kammers, S. Daly, Self-assembled nanoparticle surface patterning for improved digital image correlation in a scanning electron microscope, Exp. Mech. 53 (2013) 1333–1341.
[20] B.S. Reddy, B.N. Chatterji, An fft-based technique for translation, rotation, and scale-invariant image registration, IEEE Trans. Image Process. 5 (8) (1996) 1266–1271.
[21] H. Foroosh, J.B. Zerubia, M. Berthod, Extension of phase correlation to subpixel registration, IEEE Trans. Image Process. 11 (3) (2002) 188–200.
[22] J. Lewis, Fast normalized cross-correlation, Ind. Light Magic 10 (2001).
[23] J.-C. Yoo, T.H. Han, Fast normalized cross-correlation, Circuits, Syst. Sig. Process. 28 (2009) 819–843.
[24] H.J. Nussbaumer, The fast fourier transform, in: Fast Fourier Transform and Convolution Algorithms, Springer, 1981, pp. 80–111.
[25] G. Tzimiropoulos, V. Argyriou, S. Zafeiriou, T. Stathaki, Robust fft-based scale-invariant image registration with image gradients, IEEE Trans. Pattern Anal. Mach. Intell. 32 (10) (2010) 1899–1906.